DEVELOPMENT OF THE VASCULAR CONDITION CLASSIFIER USING SUPERVISED MACHINE LEARNING METHODS

Besedovskaia ZV[1,2] ✉, Korobov AYu[3], Kudriashova NI[4]

[1] Vladimir Zelman Center for Neurobiology and Neurorehabilitation Skolkovo Institute of Science and Technology, Moscow
[2] Artificial Intelligence Center Skolkovo Institute of Science and Technology, Moscow
[3] Center for Photonics and Photonic Technologies Skolkovo Institute of Science and Technology, Moscow
[4] Center for Molecular and Cellular Biology Skolkovo Institute of Science and Technology, Moscow

Quantitative processing of optoacoustic angiograms is an important task, the solution of which will potentially enable the early diagnosis of vascular diseases. The aim of this study is to refine and conduct biomedical validation of a software tool for the analysis of optoacoustic angiograms, focusing on the application of machine learning methods. The work was conducted on an open dataset containing three-dimensional optoacoustic angiograms of an experimental animal (mouse) in three temperature conditions: cold temperature (16 °C), room temperature (23 °C), and body temperature (30 °C), as well as a dataset with basic vascular features obtained by processing using Amira/Avizo (Thermo Fisher Scientific), a general-purpose software for visualization and analysis of scientific and industrial data. Various vascular features missing from previous work were developed and calculated, after which basic methods of unsupervised/supervised clustering and supervised classification were applied to determine different temperature conditions of vessel segments. Supervised classification methods demonstrated high overall accuracy: CatBoost — 98.9%, SGDClassifier — 95.7%, and logistic regression — 99.7%. The results are consistent with existing descriptions of vascular changes during temperature tests. The applied methodology is universal, meaning with minor modifications it can be adapted to patients. Therefore, the results of this study may potentially improve the diagnosis of vascular pathologies.

Keywords: ptoacoustics, classification, clustering of vascular changes, vasodilation, vasoconstriction, angiography, photoacoustics, vessels, vascular features

Acknowledgments: All authors of this article express their gratitude to the authors of article [15] for providing the open data used in this study.

Author contribution: Z. Besedovskaya — development of the pipeline and clustering tools, image preparation for publication, and draft publication. A. Korobov — creation and integration of new vessel segment features into the pipeline and draft publication. N. Kudryashova — medical conceptualization and validation of the vessel segment features and draft publication. All authors contributed equally to this study.

✉ **Correspondence should be addressed:** Zlata Besedovskaia
Bolshoy Bulvar, 30, Building 1, Moscow, 121205; iratnagold@gmail.com

Received: 07.10.2025 **Accepted:** 10.11.2025 **Published online:** 27.11.2025

DOI: 10.24075/brsmu.2025.060

РАЗРАБОТКА КЛАССИФИКАТОРА СОСТОЯНИЙ СОСУДОВ С ИСПОЛЬЗОВАНИЕМ МЕТОДОВ КОНТРОЛИРУЕМОГО МАШИННОГО ОБУЧЕНИЯ

З. В. Беседовская[1,2] ✉, А. Ю. Коробов[3], Н. И. Кудряшова[4]

[1] Центр нейробиологии и нейрореабилитации имени Владимира Зельмана, Сколковский институт науки и технологий, Москва, Россия
[2] Центр искусственного интеллекта, Сколковский институт науки и технологий, Москва, Россия
[3] Центр фотоники и фотонных технологий, Сколковский институт науки и технологий, Москва, Россия
[4] Центр молекулярной и клеточной биологии, Сколковский институт науки и технологий, Москва, Россия

Количественная обработка оптоакустических ангиограмм — одна из важных задач, решение которой в перспективе позволит диагностировать сосудистые заболевания на ранних стадиях. Целью исследования было провести доработку и медико-биологическую валидацию программного инструмента для анализа оптоакустических ангиограмм с фокусом на применение методов машинного обучения. Работу проводили на открытом наборе данных, содержащем трехмерные оптоакустические ангиограммы экспериментального животного (мыши) в трех температурных состояниях: температура холодной воды (16 °C), комнатная температура (23 °C) и температура тела (30 °C), а также датасет с базовыми параметрами сосудов, полученных при обработке программным обеспечением общего назначения для визуализации и анализа научных и промышленных данных Amira/Avizo (Thermo Fisher Scientific). Были разработаны и посчитаны различные параметры сосудов, отсутствующие в предыдущей работе, после чего применены основные методы неконтролируемой/контролируемой кластеризации и контролируемой классификации для определения принадлежности сегментов сосудов к разным температурным состояниям. Методы контролируемой классификации показали высокую общую точность: CatBoost — 98,9%, SGDClassifier — 95,7%, логистическая регрессия — 99,7%. Полученные результаты согласуются с существующими описаниями изменений сосудов при температурных тестах. Примененная методология универсальна, а значит при небольшой модификации может быть адаптирована для пациентов. Таким образом, полученные результаты в перспективе позволят улучшить диагностику сосудистых патологий.

Ключевые слова: оптоакустика, кластеризация васкулярных изменений, вазодилатация, вазоконстрикция, ангиография, фотоакустика

Благодарности: авторы статьи выражают признательность авторам опубликованной ранее работы [15] за предоставление открытых данных, которые были использованы при проведении исследования.

Вклад авторов: З. В. Беседовская — разработка пайплайна и инструментов кластеризации, подготовка изображений для публикации, подготовка драфта публикации; А. Ю. Коробов — создание и интеграция новых дескрипторов сегментов сосудов в пайплайн, подготовка драфта публикации; Н. И. Кудряшова — медицинская концептуализация и валидация дескрипторов сегментов сосудов, подготовка драфта публикации.

✉ **Для корреспонденции:** Злата Валерьевна Беседовская
Большой бульвар, 30, стр. 1, Москва, 121205, Россия; iratnagold@gmail.com

Статья получена: 07.10.2025 **Статья принята к печати:** 10.11.2025 **Опубликована онлайн:** 27.11.2025

DOI: 10.24075/vrgmu.2025.060

Optoacoustic (OA) angiography is a promising new vascular imaging technique applicable in scientific research and clinical practice. It is based on the optoacoustic effect: the acoustic response of materials to intermittent light [1, 2]. Thus, the method combines optical and acoustic approaches, and angiography itself is based on the optical absorption of light by hemoglobin [3].

One of the advantages of OA angiography is its noninvasive nature [1]. In diagnostics, it can complement large-vessel imaging techniques [4]. Compared to small-vessel imaging techniques (capillaroscopy, optical coherence tomography), OA provides greater visualization depth [5, 6] and enables assessment of arterioles, venules, as well as small arteries and veins [5].

OA is successfully used in various fields of both applied medicine and fundamental research. The method's successes can be highlighted in ophthalmology [7, 8], dermatology [9], cardiology [10], oncology [11], and neuroimaging [12].

Preclinical and fundamental biological research play a key role both in the study of basic biological processes and in the further development of OA imaging methodology itself [5].

Despite significant advances in the development of OA imaging technology, its widespread clinical implementation is hampered by a number of significant technological limitations. Limitations of the method include low imaging speed, a fundamental contradiction between spatial resolution and penetration depth, and engineering challenges in integrating light delivery systems and ultrasound (US) transducers [5, 6].

Artificial intelligence (AI) application is dramatically improving OA imaging. Neural networks such as U-Net effectively eliminate artifacts and improve image quality. Furthermore, AI automates data analysis, making diagnostics faster and more objective [13, 14]. Thus, the use of AI helps overcome technological barriers, enables wider clinical adoption of OA imaging, and opens new horizons for noninvasive diagnostics [5].

The goal of this work is to develop a methodology for analyzing various vascular features and validate it on an open dataset containing mouse optoacoustic 3D angiograms. The developed software will be suitable not only for the specific task described above, but also (with minor modifications) for a wide range of studies involving OA angiograms, including the diagnosis of various vascular diseases in patients.

METHODS

In this work, we used the set of features mentioned in [15] for calculations, as well as features calculated by Amira/Avizo (Thermo Fisher Scientific, USA), a general-purpose software for visualization and analysis of scientific data. We also developed new features to describe segmental spatial characteristics and improve the accuracy of machine learning (ML) models (Table 1).

Obtaining initial open data

One Balb/C nu/nu mouse was used for OA angiography. Skin vessels in the animal's left thigh were visualized in a chamber filled with distilled water. Three technical replicates were obtained (Fig. 1A) for each water temperature: body temperature (BT) (30 °C); room temperature (RT) (23 °C); and cold temperature (CT) (16 °C). Each imaging was conducted in 10 minutes after immersion of the mouse's thigh in water to stabilize the tissue and water temperatures.

An OA mesoscopy system (Institute of Applied Physics, Russian Academy of Sciences, Russia) based on an ONDA532 diode laser (wavelength 532 nm) was used for imaging. Ultrasound signals were collected using a scanning module in a sealed immersion chamber filled with distilled water. The scanning range was 10 mm in both axes, the scanning step was 20 μm, the time interval was approximately 5 min, and the signal detection depth was up to 3 mm (Fig. 1B). The acquired signals were converted into 3D angiographic datasets using reconstruction and deconvolution algorithms. The 3D angiographic images were processed using the SKYQUANT 3D tool [15].

Details of the experiment are available in a previous publication, which describes in detail the object, methods, and equipment used to acquire the images [15].

Description of the original open data

The dataset contains 16,619 vessel segments with 9 quantitative features for each segment (based on which 9 new features described in Table 1 were derived and calculated) and 11 quantitative features for each image. The experimental design is described in [15] and included:

Cold temperature (16 °C): 3 images, 10,418 segments;
Room temperature (23 °C): 3 images, 4,663 segments;
Body temperature (30 °C): 3 images, 1,538 segments.

For all subsequent operations, the original dataset was split into training, testing, and validation sets of 60%, 25%, and 15%, respectively (random seed = 42). For ML-based clustering, the features of individual segments were retained, while the features of individual images were used for descriptive statistics and quality control described in [15].

All features were standardized by removing the mean and scaling to unit variance using statistics computed only on the training samples; the same affine transformation was applied to the validation/test splits to prevent information leakage.

Unsupervised clustering based on centroid and density

Before moving on to more complex clusterers, a projection map of multidimensional objects was obtained using the nonlinear dimensionality reduction method UMAP (Uniform Manifold Approximation and Projection) with features n_neighbors = 15 and min_dist = 0.1.

After assessing visual separability of the data, K-means was applied to optimize within-cluster variance.

DBSCAN was used to capture arbitrary cluster shapes and clearly separate "noise" from the "core."

To reduce collinearity and noise while maintaining maximum variance, we applied principal component analysis (PCA) with five principal components extracted.

Following PCA, K-means and DBSCAN were repeated, and internal clustering metrics were compared.

Supervised classification

To test the separability of the data by supervised classifiers, we selected three additional models covering the linear-nonlinear and generative-discriminative families:

1. CatBoost — gradient boosting, which sequentially builds decision trees to minimize the loss function and improve the quality of the model.
2. SGDClassifier — a stochastic gradient descent learning approach that supports loss functions and penalties for classification.
3. Logistic Regression Softmax — adaptation of the logistic regression function to multiclass data.

We used a cross-validation strategy to prepare the dataset with all preprocessing. The metrics used were accuracy,

Table 1. Developed and calculated vessel features to describe the characteristics of vascular segments and their position in the image area

Feature	Formula	Description
Segment Z	Initial feature calculated automatically in Amira/Avizo software	Average depth of the centroid of segment $\mathcal{S}$
Weighted Segment MeanRadius perSegment (a.u.)	$\overline{R}_{ij_{seg}}^{(\omega)} = \frac{\overline{R}_{ij_{seg}} \bullet L_{i_{seg}}}{\sum_{i=0}^{N_j} L_{i_{seg}}}$ $\overline{R}_{ij_{seg}}$: Mean Radius i_{seg} image j; $L_{i_{seg}}$: Vessels segment Curved lenght	The mean radius value calculated for each vessel segment, weighted by the segment tortuosity or segment length
Weighted Segment Volume perSegment (a.u.)	$V_{ij_{seg}}^{(\omega)} = \frac{V_{ij_{seg}} \bullet L_{i_{seg}}}{\sum_{i=0}^{N_j} L_{i_{seg}}}$ $V_{ij_{seg}}$: Mean Radius i_{seg} image j; $L_{i_{seg}}$: Vessels segment Curved lenght	The curved length-weighted volume value calculated for each vessel segment
Features reflecting the pressure of surrounding tissues on the vessels		
Linearity	$Linearity = \frac{\lambda_1 - \lambda_2}{max(\lambda_1, \varepsilon)}$	Assesses the “threadlikeness” of a segment; values close to 1 correspond to elongated, “rod-like” structures
Planarity	$Planarity = \frac{\lambda_2 - \lambda_3}{max(\lambda_1)}$	Assesses the "ribboniness" (two-dimensionality of an object). High values are typical for geometries flattened in a plane
LinearityScore	$Linearity_{score} = \frac{\lambda_1 - \lambda_2}{\tau}$	Normalized metrics are robust to the overall Tensor scale. In practical data, LinearityScore + PlanarityScore + ScatteringScore ≈ 1
PlanarityScore	$Planarity_{score} = \frac{2 \cdot (\lambda_2 - \lambda_3)}{\tau}$	
ScatteringScore	$Scattering_{score} = \frac{3 \cdot \lambda_3}{\tau}$	
VerticalityScore	$Verticality_{score} = \lvert \upsilon_{1z} \rvert \in [0,1]$	The cosine of the angle between the main axis of the segment and the Z axis
VerticalityAngle (rad)	$Verticality_{Angle} = arccos \in [0, \pi/2]$	Angle to the Z-axis in radians

overall accuracy, balanced accuracy, logarithmic loss function Llog, Matthews correlation coefficient (MCC), Cohen's kappa (Cohen's κ), as well as ROC-AUC with macro- and micro-averaging and F1-measure with macro- and weighted averaging. Confusion matrices normalized by true classes are also presented.

RESULTS

Dimensionality reduction using the UMAP method

The UMAP method was used to visualize the multidimensional data structure.

UMAP visualization demonstrated a clear division of the data into three clusters corresponding to the three experimental temperature conditions (Fig. 2). The cold temperature cluster (16 °C) was the most compact, indicating pronounced and uniform changes in vascular architecture under hypothermia. The room temperature cluster (23 °C) occupied an intermediate position between the other two groups, while the body temperature cluster (30 °C) demonstrated a greater dispersion of points, indicating variability in vascular characteristics under physiological conditions.

Unsupervised clustering

To evaluate the effectiveness of unsupervised ML methods in the problem of separating temperature states, the DBSCAN and K-Means algorithms were used both with and without PCA data preprocessing (Table 2).

An analysis of the results showed that the use of PCA did not significantly improve clustering quality. The DBSCAN algorithm demonstrated higher accuracy (0.626) and silhouette coefficient (0.632) compared to K-Means, but showed low values of the macro-averaged F1-measure ($F1_{macro}$) (0.259), indicating unbalanced class recognition. K-Means, in contrast, provided a better balance between classes ($F1_{macro} = 0.367$), but with lower overall accuracy (0.524). The extremely low values of

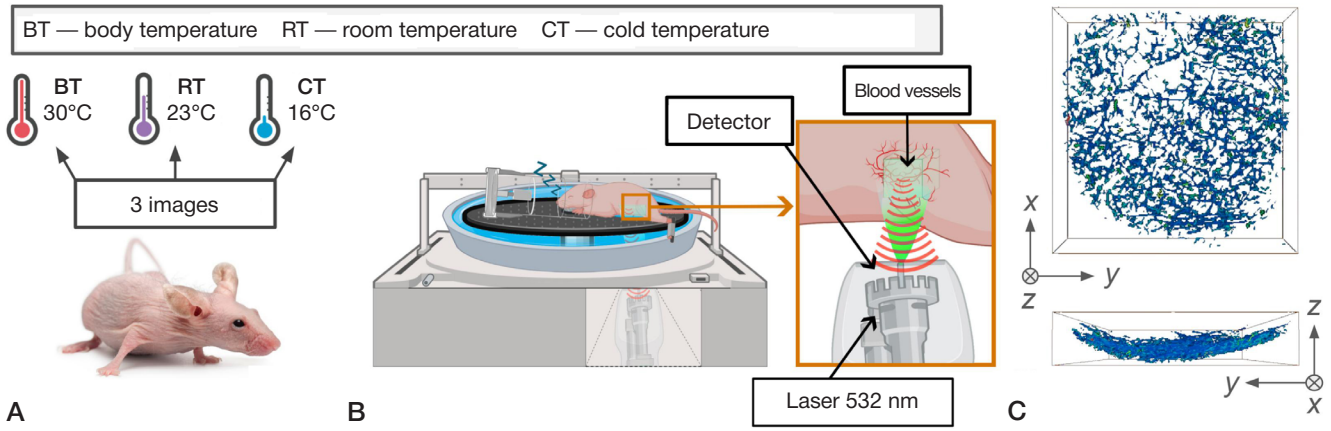

Fig. 1. A. Schematic representation of the experimental design. **B**. Schematic representation of the experimental setup. **C**. Image in the analyzed coordinate plane. Modified from [15]

the adjusted Rand index (ARI < 0.015) and normalized mutual information (NMI < 0.02) for both algorithms indicate a weak correspondence between the resulting clusters and the true temperature groups when using unsupervised approaches.

Despite multi-stage training, the internal clustering evaluation metrics demonstrated insufficient consistency and stability for subsequent interpretation.

Supervised Classification

Classification with the Catboost Model

To solve the problem of supervised classification of temperature states, gradient boosting on decision trees in the Catboost implementation was applied. The classification results are presented in Fig. 2B.

The Catboost model demonstrated exceptional performance in classifying temperature states in the vascular network. Overall accuracy was 98.9%, with a balanced accuracy of 98.5%, indicating correct model performance even with varying numbers of observations in classes. The area under the ROC curve, exceeding 0.999 for all averaging variants, indicates near-perfect separability of the classes in the feature space.

The highest classification recall (recall = 0.997) was achieved for the cold temperature group, consistent with the results of the UMAP analysis, which showed the greatest compactness and isolation of this cluster. The body temperature group demonstrated the highest accuracy (precision = 0.997), but slightly lower recall (0.985). The lowest completeness was observed for the room temperature group (0.971), which may be associated with the transitional nature of this state between hypo- and normothermia.

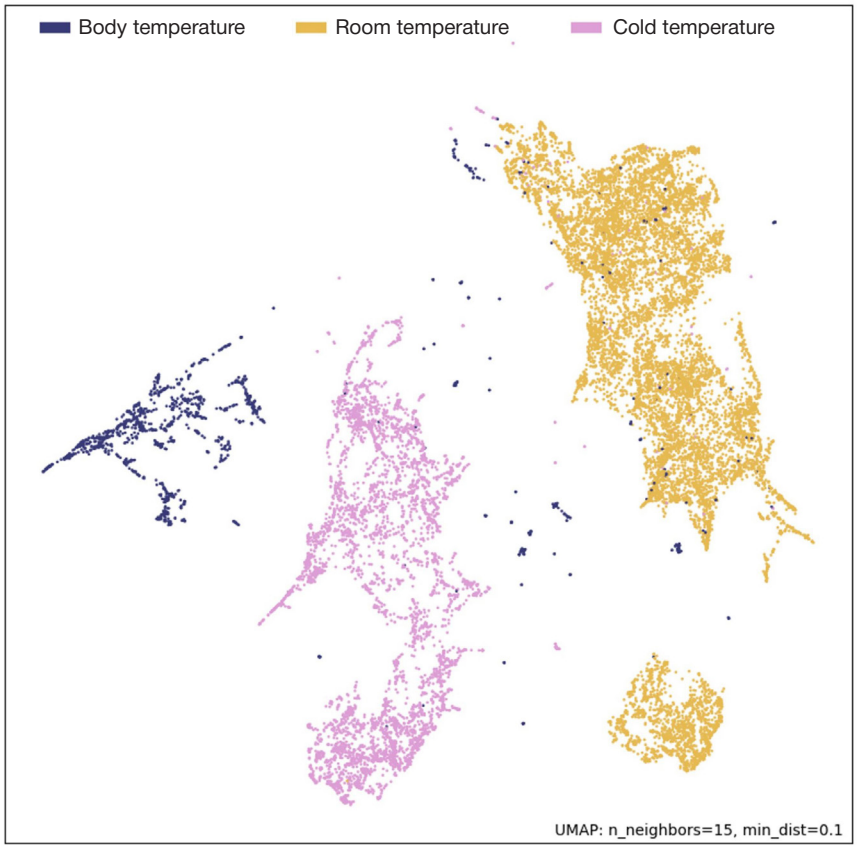

Fig. 2. UMAP clustering of the original data

Table 2. Obtained metrics of unsupervised clustering

Metrics	K-Means	DBSCAN	K-Means (PCA)	DBSCAN (PCA)
accuracy	0.524	0.626	0.524	0.626
$F1_{macro}$	0.367	0.259	0.367	0.259
silhouette	0.326	0.632	0.333	0.628
ARI	0.014	0.005	0.014	0.004
NMI	0.017	0.002	0.017	0.001

Classification by the SGDClassifier model

The SGDClassifier model demonstrated robust performance on the test set (Table 3): overall accuracy was 95.7%, balanced accuracy was 95.1%, $F1_{macro}$ was 0.960, and $F1_{weighted}$ was 0.956. The goodness-of-fit coefficients were also high (MCC = 0.917, Cohen's κ = 0.915), indicating reliable prediction consistency above chance. The area under the ROC curve was high (macro-AUC = 0.988; micro-AUC = 0.994), but it still performed worse than the nonlinear gradient boosting model; the log loss of 0.176 indicates a more conservative probabilities calibration compared to the Catboost model.

Very high recall (recall = 0.997) and very high precision (precision = 0.994) were shown for the body temperature group (F1 = 0.997), indicating clear separability of this condition in the space of all features. For the cold temperature group, the model demonstrated record sensitivity (recall = 0.995) simultaneously with moderately reduced precision (precision = 0.940; F1 = 0.967). The greatest clustering difficulties, as in the previous case, were shown for the room temperature group: despite high precision (precision = 0.988), the recall is shown below (recall = 0.857; F1 = 0.918), indicating frequent assignments of objects from this group to neighboring groups, primarily to the cold temperature group. This effect is typical of linear separators in the case of a transitional class.

Classification by logistic regression model

The logistic regression model, like Catboost, demonstrated near-limit performance on the test set (Table 3). The area under the ROC curve is close to ideal ($ROC\text{-}AUC_{macro}$ = 0.99983; $ROC\text{-}AUC_{micro}$ = 0.99987), while the low logarithmic loss (L_{log} = 0.033) indicates good calibration of the probabilities—better than the other linear and boosted models.

For the body temperature group, extremely high recall values (recall = 0.996) with very high precision (precision = 0.998; F1 = 0.999) are shown, indicating good separability of this condition. For the cold temperature group, the quality is also close to ideal (precision = 0.999; recall = 0.997; F1 = 0.998), meaning that the model makes virtually no errors in classifying segments from images in the cold temperature group. The greatest decrease is observed for the room temperature group: precision = 0.993, recall = 0.996, F1 = 0.995. This indicates rare false positives in favor of the room temperature group for boundary objects.

Assessing the significance of features for three models revealed two stable, highly significant classes (Fig. 3A): topological (tortuosity, verticality/planarity, normalized dispersion, and linearity) and geometric (radii, lengths, volume, and segment Z-coordinate). It is important to note that the linear models (SGDClassifier and logistic regression) base their decisions primarily on topological features.

The confusion matrix (Fig. 3B) allows for a detailed assessment of misclassification patterns for the three models.

For logistic regression, the significance of tortuosity (Fig. 3A) is noteworthy, with its contribution exceeding that of the other features by an order of magnitude. Smaller but consistent contributions are provided by normalized verticality, normalized linearity, planarity, verticality angle, normalized dispersion, and linearity (approximately 0.28–1.07). The scale features — mean radii, length/tortuosity-weighted mean radii, curved and cord length, volume and weighted volume, and segment z-coordinate — are of virtually zero importance.

SGDClassifier follows the same linear weighting pattern: the tortuosity feature contributes the most, followed by normalized verticality, planarity, verticality angle, normalized scattering, and linearity; geometric features remain close to zero.

Unlike linear models, the Catboost model exhibits a different feature hierarchy: the tortuosity-weighted mean radius, volume, and curved length are of maximum importance. Topological features such as tortuosity make a minor contribution.

DISCUSSION

A standard approach for analyzing OA imaging results is the use of AI methods [13]. An example is the work of N. Davoudi et al., who used the U-Net neural network to improve the quality of images distorted by artifacts. The authors trained the model on a hybrid dataset that included simulations, phantoms, and

Table 3. Metrics for assessing the quality of supervised classification models

Метрика	Catboost	LogisticRegression	SGDClassifier
accuracy	0.989	0.997	0.957
balanced accuracy	0.985	0.998	0.951
L_{log}	0.108	0.033	0.176
MCC	0.979	0.994	0.917
Cohen's κ	0.979	0.994	0.915
$ROC\text{-}AUC_{macro}$	0.999	0.999	0.988
$F1_{macro}$	0.988	0.997	0.96
$ROC\text{-}AUC_{micro}$	0.999	0.999	0.994
$F1_{weighted}$	0.989	0.997	0.956

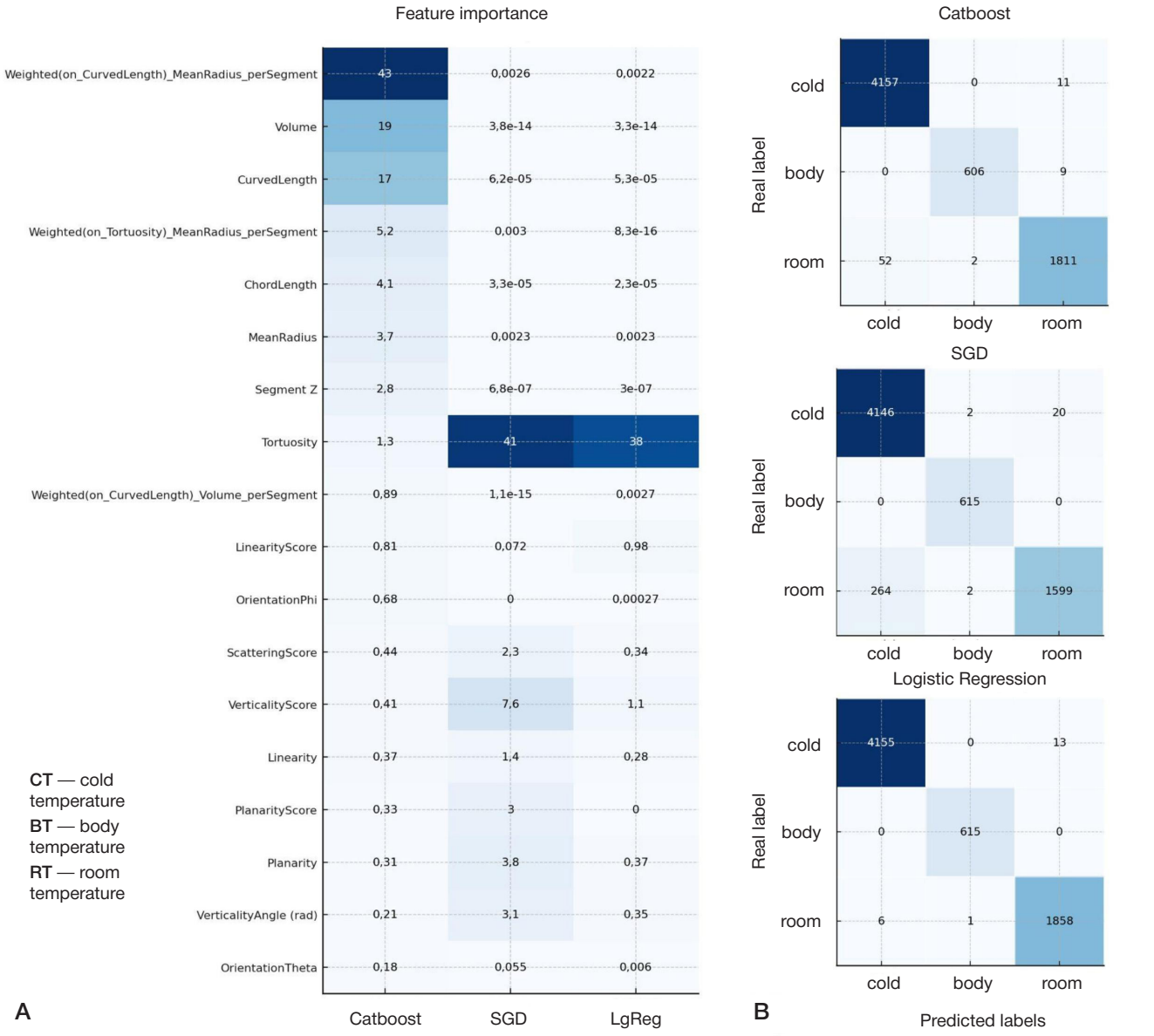

Fig. 3. Characteristics of trained ML models: Catboost, SGDClassifier, LogisticRegression. **A**) Feature weights for individual vessel segments. **B**) Error matrices for the three models

cross-sectional images of mice *in vivo*. The trained network effectively removed artifacts even with a sixfold undersampling of the original data. Validation on an experimental setup confirmed that the algorithm successfully copes with the task, significantly improving image quality [14]. However, it is worth considering that the main limiting factor for the use of artificial intelligence methods is the amount of data being analyzed [16]. In our study, unlike the aforementioned studies, we were able to overcome the data limitation by using a hybrid approach: image filtering and extraction of the analyzed vascular features are performed using a modified SKYQUANT-3D pipeline [15], which does not employ machine learning methods. However, further analysis was performed using various machine learning classifiers and clusterers. The effectiveness of the SKYQUANT-3D pipeline methodology has already been confirmed in tests on a vascular phantom, preclinical experiments, and clinical experiments [15].

The most important step in the analysis of OA angiograms is the selection and calculation of the analyzed vascular features. For example, in [17], 64 microvascular features were obtained, characterizing vessel blood flow, changes in their geometric configuration, branching, spatial localization, and other features [17]. The authors of the study used a random forest-based classifier for feature selection in order to identify the most significant biomarkers from the initial 64 features. By reducing the dataset to 32 key features, they were able to focus on the most informative features for differentiating healthy volunteers from diabetic patients, thereby confirming the importance of selecting significant vascular features for further analysis [17].

In [18], visual assessment of vascular features such as diameter and tortuosity was performed, which enabled effective discrimination between patients with post-thrombotic syndrome and healthy volunteers [18]. In the study [15], vessel radii, lengths, and tortuosity were analyzed in various variations. This made it possible to characterize changes in the vessels of an experimental animal during a temperature test, as well as changes in the vessels of a healthy volunteer during a positional test [15]. Our study uses the features from the article [15], supplementing them with features of branching and spatial localization similar to those mentioned in [17]. The unique features of vessel planarity, verticality, and linearity also deserve

special attention, indicating changes in the microcirculatory bed due to fluid redistribution. In this experiment, fluid redistribution in the body of the experimental animal was associated with temperature changes, but similar processes can occur in humans as a result of the development of vascular disease, such as chronic venous insufficiency [19].

The feature values we obtained reflect changes in the vessels caused by cooling, previously shown by other authors. Cooling causes dilation of small peripheral vessels, leading to a greater volume of blood containing hemoglobin, the main source of contrast in optoacoustics, to pass through them [20–22]. This makes them "visible" to the imaging system. The overall increase in blood volume in the studied area is a direct consequence of the vasodilation process. The peripheral vascular network is inherently more tortuous and branched than the main vessels, so its visibility in the image leads to an increase in the mean tortuosity feature [20–22]. Thus, the effectiveness of the classification is explained by existing biological effects. It is worth noting that many of the analysis components are universal for both animals and humans, which allows the development to be implemented into clinical practice.

CONCLUSIONS

In this study, quantitative vascular features were calculated and analyzed to describe the state of the microcirculatory bed.

Various machine learning methods were compared for determining different temperature states in experimental animals. Supervised classification methods demonstrated the greatest effectiveness, with near-absolute accuracy. The Catboost and logistic regression models demonstrated the greatest success, accounting for the most significant physiological features. Further, the choice between the two models should be made on a case-by-case basis, depending on the specific feature distribution. Feature weights reflect the actual physiology of vascular changes.

The methodology developed in this study will potentially help not only effectively distinguish between experimental conditions but also differentiate pathological vascular changes from each other and from the norm in patients with various diseases. This will help overcome some of the limitations of OA angiography, enabling its wider implementation in clinical practice. This will enable more accurate diagnosis of vascular changes in the early stages of diseases.

References

1. Lin L, Wang LV. The emerging role of photoacoustic imaging in clinical oncology. Nat Rev Clin Oncol. 2022; 19: 365–384. DOI: 10.1038/s41571-022-00615-3.
2. Neprokin A, Broadway C, Myllylä T, Bykov A, Meglinski I. Photoacoustic Imaging in Biomedicine and Life Sciences. Life. 2022; 12: 588. DOI: 10.3390/life12040588.
3. Xia J, Yao J, Wang LHV. Photoacoustic tomography: principles and advances. PIER. 2014; 147: 1–22. DOI: 10.2528/pier14032303.
4. Karlas A, Fasoula N-A, Paul-Yuan K, Reber J, Kallmayer M, Bozhko D, et al. Cardiovascular optoacoustics: From mice to men — A review. Photoacoustics. 2019; 14: 19–30. DOI: 10.1016/j.pacs.2019.03.001.
5. Kye H, Song Y, Ninjbadgar T, Kim C, Kim J. Whole-Body Photoacoustic Imaging Techniques for Preclinical Small Animal Studies. Sensors. 2022; 22: 5130. DOI: 10.3390/s22145130.
6. Wang X, Ku G, Wegiel MA, Bornhop DJ, Stoica G, Wang LV. Noninvasive photoacoustic angiography of animal brains in vivo with near-infrared light and an optical contrast agent. Opt Lett. 2004; 29: 730. DOI: 10.1364/ol.29.000730.
7. Hu S, Rao B, Maslov K, Wang LV. Label-free photoacoustic ophthalmic angiography. Opt Lett. 2009; 35: 1. DOI: 10.1364/ol.35.000001.
8. Zhao H, Li K, Yang F, Zhou W, Chen N, et al. Customized anterior segment photoacoustic imaging for ophthalmic burn evaluation in vivo; OEA. 2021; 4: 200017–200017. DOI: 10.29026/oea.2021.200017.
9. Li D, Humayun L, Vienneau E, Vu T, Yao J. Seeing through the Skin: Photoacoustic Tomography of Skin Vasculature and Beyond. JID Innovations. 2021; 1: 100039. DOI: 10.1016/j.xjidi.2021.100039.
10. Luo Y, Wang LV. Photoacoustic Tomography in Cardiovascular Medicine: Innovations in Assessing Hemodynamics and Metabolic Function. Curr Treat Options Cardio Med. 2025; 27. DOI: 10.1007/s11936-025-01092-4.
11. Leng X, Uddin KMS, Chapman W Jr, Luo H, Kou S, Amidi E, et al. Assessing Rectal Cancer Treatment Response Using Coregistered Endorectal Photoacoustic and US Imaging Paired with Deep Learning. Radiology. 2021; 299: 349–358. DOI: 10.1148/radiol.2021202208.
12. Qiu T, Lan Y, Gao W, Zhou M, Liu S, Huang W, et al. Photoacoustic imaging as a highly efficient and precise imaging strategy for the evaluation of brain diseases. Quant Imaging Med Surg. 2021; 11: 2169–86. DOI: 10.21037/qims-20-845.
13. Brown EL, Lefebvre TL, Sweeney PW, Stolz BJ, Gröhl J, Hacker L, et al. Quantification of vascular networks in photoacoustic mesoscopy. Photoacoustics. 2022; 26: 100357. DOI: 10.1016/j.pacs.2022.100357.
14. Davoudi N, Deán-Ben XL, Razansky D. Deep learning optoacoustic tomography with sparse data. Nat Mach Intell. 2019; 1: 453–60. DOI: 10.1038/s42256-019-0095-3.
15. Korobov A, Besedovskaia Z, Petrova E, Kurnikov A, Glyavina A, Orlova A, et al. SKYQUANT 3D: Quantifying Vascular Anatomy With an Open-Source Workflow for Comprehensive Analysis of Volumetric Optoacoustic Angiography Data. Journal of Biophotonics. 2024; 17. DOI: 10.1002/jbio.202400143.
16. Baeza-Yates R. The Limitations of Data, Machine Learning and Us. Companion of the 2024 International Conference on Management of Data. ACM; 2024. pp. 1–2. DOI: 10.1145/3626246.3656000.
17. Karlas A, Katsouli N, Fasoula N-A, Bariotakis M, Chlis N-K, Omar M, et al. Dermal features derived from optoacoustic tomograms via machine learning correlate microangiopathy phenotypes with diabetes stage. Nat Biomed Eng. 2023; 7: 1667–82. DOI: 10.1038/s41551-023-01151-w.
18. Nemirova S, Orlova A, Kurnikov A, Litvinova Y, Kazakov V, Ayvazyan I, et al. Scanning optoacoustic angiography for assessing structural and functional alterations in superficial vasculature of patients with post-thrombotic syndrome: A pilot study. Photoacoustics. 2024; 38: 100616. DOI: 10.1016/j.pacs.2024.100616.
19. Barajas Colón JÁ, Granados-Romero JJ, Barrera-Mera B, Banegas-Ruiz R, Vargas-Morales JJ, Barrera-Calva E, et al. Chronic venous insufficiency: a review. Int J Res Med Sci. 2021; 9: 1808. DOI: 10.18203/2320-6012.ijrms20211928.
20. Zhang R, Li X, Balasundaram G, Li B, Qi Y, Santosa A, et al. Hybrid Photoacoustic Ultrasound Imaging System for Cold-Induced Vasoconstriction and Vasodilation Monitoring. IEEE Trans Biomed Eng. 2024; 71: 712–6. DOI: 10.1109/tbme.2023.3301013.
21. Chang F, Flavahan S, Flavahan NA. Cooling-induced cutaneous vasodilatation is mediated by small-conductance, calcium-activated potassium channels in tail arteries from male mice. Physiological Reports. 2023; 11. DOI: 10.14814/phy2.15884.
22. Van den Brande P, De Coninck A, Lievens P. Skin Microcirculation Responses to Severe Local Cooling. Int J Microcirc. 1997; 17: 55–60. DOI: 10.1159/000179207.

Литература

1. Lin L, Wang LV. The emerging role of photoacoustic imaging in clinical oncology. Nat Rev Clin Oncol. 2022; 19: 365–384. DOI: 10.1038/s41571-022-00615-3.
2. Neprokin A, Broadway C, Myllylä T, Bykov A, Meglinski I. Photoacoustic Imaging in Biomedicine and Life Sciences. Life. 2022; 12: 588. DOI: 10.3390/life12040588.
3. Xia J, Yao J, Wang LHV. Photoacoustic tomography: principles and advances. PIER. 2014; 147: 1–22. DOI: 10.2528/pier14032303.
4. Karlas A, Fasoula N-A, Paul-Yuan K, Reber J, Kallmayer M, Bozhko D, et al. Cardiovascular optoacoustics: From mice to men — A review. Photoacoustics. 2019; 14: 19–30. DOI: 10.1016/j.pacs.2019.03.001.
5. Kye H, Song Y, Ninjbadgar T, Kim C, Kim J. Whole-Body Photoacoustic Imaging Techniques for Preclinical Small Animal Studies. Sensors. 2022; 22: 5130. DOI: 10.3390/s22145130.
6. Wang X, Ku G, Wegiel MA, Bornhop DJ, Stoica G, Wang LV. Noninvasive photoacoustic angiography of animal brains in vivo with near-infrared light and an optical contrast agent. Opt Lett. 2004; 29: 730. DOI: 10.1364/ol.29.000730.
7. Hu S, Rao B, Maslov K, Wang LV. Label-free photoacoustic ophthalmic angiography. Opt Lett. 2009; 35: 1. DOI: 10.1364/ol.35.000001.
8. Zhao H, Li K, Yang F, Zhou W, Chen N, et al. Customized anterior segment photoacoustic imaging for ophthalmic burn evaluation in vivo; OEA. 2021; 4: 200017–200017. DOI: 10.29026/oea.2021.200017.
9. Li D, Humayun L, Vienneau E, Vu T, Yao J. Seeing through the Skin: Photoacoustic Tomography of Skin Vasculature and Beyond. JID Innovations. 2021; 1: 100039. DOI: 10.1016/j.xjidi.2021.100039.
10. Luo Y, Wang LV. Photoacoustic Tomography in Cardiovascular Medicine: Innovations in Assessing Hemodynamics and Metabolic Function. Curr Treat Options Cardio Med. 2025; 27. DOI: 10.1007/s11936-025-01092-4.
11. Leng X, Uddin KMS, Chapman W Jr, Luo H, Kou S, Amidi E, et al. Assessing Rectal Cancer Treatment Response Using Coregistered Endorectal Photoacoustic and US Imaging Paired with Deep Learning. Radiology. 2021; 299: 349–358. DOI: 10.1148/radiol.2021202208.
12. Qiu T, Lan Y, Gao W, Zhou M, Liu S, Huang W, et al. Photoacoustic imaging as a highly efficient and precise imaging strategy for the evaluation of brain diseases. Quant Imaging Med Surg. 2021; 11: 2169–86. DOI: 10.21037/qims-20-845.
13. Brown EL, Lefebvre TL, Sweeney PW, Stolz BJ, Gröhl J, Hacker L, et al. Quantification of vascular networks in photoacoustic mesoscopy. Photoacoustics. 2022; 26: 100357. DOI: 10.1016/j.pacs.2022.100357.
14. Davoudi N, Deán-Ben XL, Razansky D. Deep learning optoacoustic tomography with sparse data. Nat Mach Intell. 2019; 1: 453–60. DOI: 10.1038/s42256-019-0095-3.
15. Korobov A, Besedovskaia Z, Petrova E, Kurnikov A, Glyavina A, Orlova A, et al. SKYQUANT 3D: Quantifying Vascular Anatomy With an Open-Source Workflow for Comprehensive Analysis of Volumetric Optoacoustic Angiography Data. Journal of Biophotonics. 2024; 17. DOI: 10.1002/jbio.202400143.
16. Baeza-Yates R. The Limitations of Data, Machine Learning and Us. Companion of the 2024 International Conference on Management of Data. ACM; 2024. pp. 1–2. DOI: 10.1145/3626246.3656000.
17. Karlas A, Katsouli N, Fasoula N-A, Bariotakis M, Chlis N-K, Omar M, et al. Dermal features derived from optoacoustic tomograms via machine learning correlate microangiopathy phenotypes with diabetes stage. Nat Biomed Eng. 2023; 7: 1667–82. DOI: 10.1038/s41551-023-01151-w.
18. Nemirova S, Orlova A, Kurnikov A, Litvinova Y, Kazakov V, Ayvazyan I, et al. Scanning optoacoustic angiography for assessing structural and functional alterations in superficial vasculature of patients with post-thrombotic syndrome: A pilot study. Photoacoustics. 2024; 38: 100616. DOI: 10.1016/j.pacs.2024.100616.
19. Barajas Colón JÁ, Granados-Romero JJ, Barrera-Mera B, Banegas-Ruiz R, Vargas-Morales JJ, Barrera-Calva E, et al. Chronic venous insufficiency: a review. Int J Res Med Sci. 2021; 9: 1808. DOI: 10.18203/2320-6012.ijrms20211928.
20. Zhang R, Li X, Balasundaram G, Li B, Qi Y, Santosa A, et al. Hybrid Photoacoustic Ultrasound Imaging System for Cold-Induced Vasoconstriction and Vasodilation Monitoring. IEEE Trans Biomed Eng. 2024; 71: 712–6. DOI: 10.1109/tbme.2023.3301013.
21. Chang F, Flavahan S, Flavahan NA. Cooling-induced cutaneous vasodilatation is mediated by small-conductance, calcium-activated potassium channels in tail arteries from male mice. Physiological Reports. 2023; 11. DOI: 10.14814/phy2.15884.
22. Van den Brande P, De Coninck A, Lievens P. Skin Microcirculation Responses to Severe Local Cooling. Int J Microcirc. 1997; 17: 55–60. DOI: 10.1159/000179207.